2024 IEEE International Conference on Robotics and Automation (ICRA 2024)
May 13-17, 2024. Yokohama, Japan

Representing On-Orbit Rendezvous and Proximity Operations with Fully-Actuated Multirotor Aerial Platforms

Alessandro Garzelli*, Kumud Darshan Yadav*, Alessandro Scalvini*, Antonio Gonzalez-Morgado*, Alejandro Suarez* and Anibal Ollero*, *IEEE Fellow*

***Abstract*— Ground testing is of paramount importance to verify and validate space operations and the associated control algorithms before on-orbit deployment. Although state-of-the-art facilities are capable of reproducing zero-G environment with high degree of fidelity, these infrastructures can be complemented with multi-rotors emulating free flying or free floating conditions, exploiting the similarities and analogies between both domains in terms of floating nature, attitude dynamics, and thrust-wrench relation through the mixer matrix. Furthermore, the effective workspace of the testbed can be extended to the dimensions of the flight area and the coverage of the positioning system. Therefore, this papers introduces a new way to recreate orbital motion within an indoor facility, considering the case study of trajectories derived from the Clohessy–Wiltshire equations. This advancement opens up avenues for replicating close-proximity operations between chaser and target satellites employing fully-actuated multi-rotors that allow decoupling translational and attitude dynamics.**

I. INTRODUCTION

On-orbit maintenance operations are needed in today's era to mitigate the numerous challenges and hazards encountered during nominal operation in space. Such operations typically involve executing complex on-orbit maneuvers, which remains essential for establishing a sustainable and economically viable space program. The scientific community is devoting considerable resources to study complex tasks such as on-orbit inspection [1], servicing [2], assembly of space structures [3] [4], refueling [5] and debris removal [6]. Regardless of the specific mission, the spacecraft has to perform certain rendezvous maneuvers for specific cases. This entails the chaser spacecraft executing a rendezvous and approaching maneuver to attain the necessary attitude and proximity to the target to perform its predesignated task, such as inspection. This maneuver also demands the chaser spacecraft to approach the target in close quarters, introducing the risk of unexpected and uncontrolled collisions. The specific mission cases which involves docking needs to be dealt with care if the inertia properties of two spacecrafts are comparable, because of abrupt change in inertia properties of the combined platforms may result in unstable attitude dynamics. Given the severity of the repercussions stemming from unforeseen collisions [7], it is evident that these maneuvers are exceptionally delicate. They demand meticulous design, rigorous testing in both simulation and hardware-in-the-loop test-beds [8], [9], [10], [11], before being ready for actual on-orbit deployment.

*Authors are with the GRVC Robotics Lab, School of Engineers, University of Seville, Spain https://grvc.us.es/

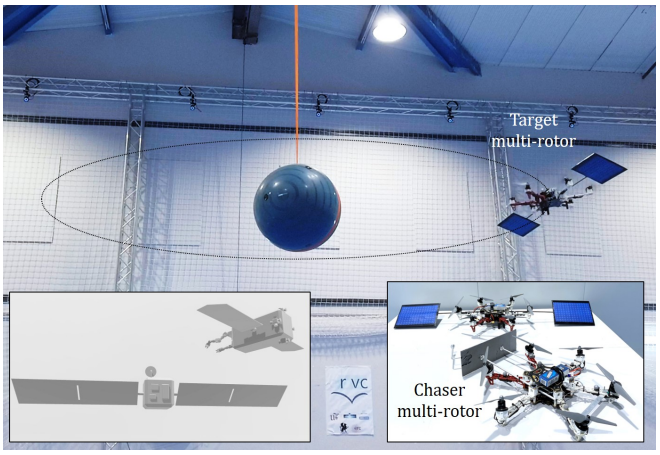

Fig. 1. Fully actuated multi-rotor conducting an orbital flight in an indoor testbed, using two platforms for simulating a proximity operation between a target and a chaser, this one equipped with a mockup of dual arm.

Micro-gravity simulations are a crucial aspect for space flight validation, and various innovative testbeds have been developed to replicate the conditions of space environment [12][13]. Air bearings [11] employ a cushion of air to suspend objects, thus allowing to simulate a quasi frictionless movement, partially mimicking the environment experienced in space. The primary categories of air bearings are planar bearings, which are employed to replicate translational motion, and gyroscopic bearings, designed to mimic changes in attitude [14]. On the other hand, industrial manipulators equipped with precise high-bandwidth controllers are commonly employed to emulate the free-floating/free-flying dynamics of the satellite [15], [16], [8]. The robotic system works on the principle of rigid body kinematics and dynamics to reproduce a 6D (translation and rotation) trajectory integrating the actual dynamics of the satellite in the space domain [17]. Other interesting approaches which have been followed to generate the near space condition are the Neutral Buoyancy Facilities[18] and the less popular strategies such as Parabolic and Free Fall flights, which are capable of reducing the gravity to $0.02g$ and $0.001g$, respectively, for a duration of approximately 10 - 20 seconds [19].

The use of multi-rotor platforms, particularly those providing fully actuated [20], [21], [22], [23] or omnidirectional [24], [25] motion capability, shows great potential to simulate orbital flight due to the possibility to decouple attitude and translational dynamics by the convenient arrangement of the propellers [26]. Such cases of replicating free flying/floating

trajectories have been considered in few works [27], [28], [25]. However, [28] is more focused on the synthesis of images and perception methods for the detection of space components, presenting basic flight tests in simulated Mars environment, whereas [25] considers the controller design in Simulink, without reporting real flight data. The work presented in [27] presents a prototype of an omni-directional platform and preliminary validating experiments. Motivated by the recent advancement in the drone technology, which have made it a viable and cost-effective solution to use it as a test-bed for conducting and validatig space technologies, this paper explores the potential use of drones to emulate the near zero-G conditions, extending the capabilities of current testbeds [29], [30], [31] . The main novelties of the current scope of work are therefore the following:

- Using fully actuated multi-rotors to simulate micro-gravity conditions on free flying/free floating conditions.
- The incorporation of the equations of motion of orbital mechanics to be implemented by the multi-rotor.
- The comparison of the aerial and spacecraft dynamics, and the identification of practical simulation aspects.
- A road-map of possible applications of the experimental testbed to simulate rendezvous and target inspection.

The paper is organized as follows. Section II introduces the notation and presents the intended problem. Section III derives the equations of motion of the orbital flight, specifically during the final phase of a rendezvous, whereas Section IV is focused on the fully-actuated multi-rotor. Section V presents the numerical simulation and the experimental results. Finally, the conclusions and future work are summarized in Section VI.

II. PROBLEM FORMULATION

A. Notation

The following notation, based on [32], will be used in the rest of the paper to represent the different parameters involved in the representation of the orbital flight both in the aerial and space domains:

- $\boldsymbol{I}_{\oplus} = \hat{X}\hat{Y}\hat{Z}$: Earth Centered Inertial frame (ECI).
- $\boldsymbol{I}_{LVLH} = \hat{i}\hat{j}\hat{k}$: Local-Vertical-Local-Horizontal frame (LVLH).
- $\boldsymbol{I}_{tb}$ = right handed orthonormal reference frame centered onto the CoM (center of mass) of the target, aligned with the principal axes of inertia of the body.
- $\boldsymbol{I}_{cb}$ = right handed orthonormal reference frame centered onto the CoM of the chaser, aligned with the principal axes of inertia of the body.
- $\boldsymbol{T}$ = matrix for the reduced kinematic equation as defined in [33].
- $\boldsymbol{R}, \boldsymbol{r}$: Position of the target and chaser orbits respectively in $\boldsymbol{I}_{\oplus}$ $[km]$.
- $\delta\boldsymbol{r}$: Relative position vector between the chaser and the target $[km]$.
- $\boldsymbol{V}, \boldsymbol{v}$: Orbital flight speed of target and chaser $[km/s]$.
- θ: True anomaly of the target $[rad/s]$.
- m_c, m_t: Mass of the chaser and target spacecraft $[kg]$.
- $\boldsymbol{J}_c, \boldsymbol{J}_t$: Inertia matrix of chaser and target respectively.
- μ : Gravitational parameter of Earth in $\left[km^3/s^2\right]$.

B. Simulation of Orbital Flight

As depicted in Figure 2, the paper considers the problem of simulating the relative motion of the a chaser satellite with respect to the target. The simulation is performed using an indoor test-bed with fully actuated multi-rotors [20], [22], [23] given their ability to decouple the translational from the rotational dynamics. Relying on the analogy between propellers and thrusters and on the autopilot controller it is possible to simulate the attitude (full range in yaw, and limited to $\pm 10^{\circ}$ in roll and pitch [23]) and the orbital trajectory of the space vehicle. The scenario comprises two platforms: a hovering multi-rotor representing a target satellite, equipped with a solar array, and another multi-rotor playing the role of the chaser. The flight tests are carried out in the GRVC Robotics Laboratory testbed, providing $20 \times 15 \times 8$ m flight workspace, equipped with 28 Opti-Track cameras to provide accurate position and orientation measurements. This is shown in Figure 1.The aerial platform, also shown in Figure 1, consists of a modified F550 hexarotor, introducing 3D printed plastic frames to achieve the rotation of the propellers for the fully actuated configuration. The flight controller is implemented in a Cube v5 autopilot with Ardupilot firmware. This setup is widely used in aerial robotics research, which motivates its choice. This testing system allows to simulate orbital trajectories linked to proximity operations.

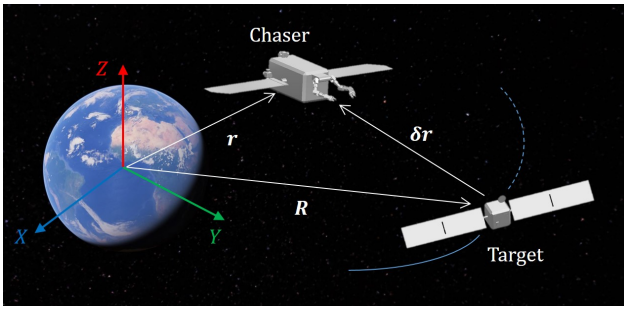

Fig. 2. Schematic representation of the initial rendezvous configuration

C. Similarities and Differences Between Aerial and Space Platforms

The suitability of fully-actuated [22] or omnidirectional [27], [24], [25] multi-rotors for simulating rendezvous and proximity operations between two on-orbit platforms (target satellite and chaser) is motivated by the significant similarities between both kind of platforms in the following terms:

- Attitude and translational dynamics/control are decoupled due to the convenient arrangement of the propellers that allow generating 6-DOF wrenches [34].
- Propellers and thrusters can be assimilated to unidirectional thrust vectoring actuators, obtaining the generated body wrenches through the Mixer Matrix.
- Both kind of platforms implement attitude controllers.

However, major differences can be also identified, mainly:

- Aerial platforms must compensate gravity, devoting most of their energy to it, whereas space platforms are inserted at a certain altitude from the surface of the Earth by a launcher and acquire an orbital shape given an initial state vector that comprehends the coordinates of the space platform $\boldsymbol{R}$ and its velocity $\boldsymbol{V}$ [32].
- Aerodynamic effects like the downwash [35] impose a minimum separation distance between multi-rotors, as represented in Figure 3.
- Multi-rotor propellers introduce significant vibrations affecting the Inertial Measurement Unit (IMU), particularly the accelerometer, and consequently the accuracy of the attitude and position controllers. This requires filtering and sensor fusion techniques, typically an Extended Kalman Filter (EKF) [36].
- Differences in mass, inertia, or speed unavoidably arise unless the satellites to be represented are in the scale of CubeSats, requiring appropriate dimensional analysis to address this [37], [38].

Note that gravity compensation is an inherent problem in the replication of free flying/floating dynamics in ground testbeds, being a typical feature of industrial robot arms [15]. In the simulation of rendezvous and proximity operations using the two multi-rotors (target and chaser) it is necessary to account for the two constraints depicted in Figure 3: 1) the minimum separation distance for collision avoidance, and 2) the aerodynamic downwash effect between the propellers of the two platforms (studied in our previous work [39]), indicating the valid and invalid approaching maneuvers according to the minimum horizontal and vertical separation distances, D_{min} and H_{min}, respectively. The first parameter is determined by the tip-to-tip size of the multi-rotor and a safety margin (around 50% of this), whereas the second one can be roughly determined from aerodynamic blade theory [39], in a way that the thrust increase experienced by the lower multi-rotor to compensate the downwash effect is lower than the 10 - 20% of its nominal thrust. In this work, the proximity operation is conducted respecting the horizontal distance D_{min} that avoids the downwash effect and allows to get both platforms close enough for a docking.

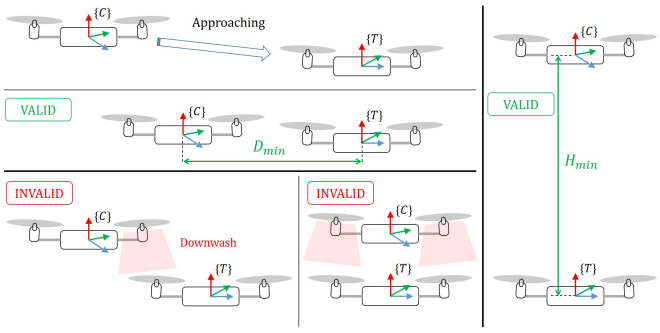

Fig. 3. Valid and invalid approaching maneuvers of chaser and target multi-rotors simulating the space platforms, taking into account the aerodynamic downwash and collision avoidance constraints imposing a minimum horizontal and vertical distances D_{min} and H_{min}, respectively.

III. ORBITAL FLIGHT MODEL

A. Translational Dynamics

The model considered here is depicted in Figure 2. The Earth reference frame $\boldsymbol{I}_{\oplus}$ has the $\hat{X}$ and $\hat{Y}$ axes on the equatorial plane with the $\hat{X}$ axis pointing at the vernal Equinox [40]. The $\hat{Z}$ axis is perpendicular to the$\hat{X}\hat{Y}$ plane. The vector $\mathbf{R}$ connects the center of the origin of $\boldsymbol{I}_{\oplus}$ with the CoM of target, whereas $\mathbf{r}$ is the vector from the origin of $\boldsymbol{I}_{\oplus}$ to the CoM of the chaser. The orbital frame coincides with the $\boldsymbol{I}_{LVLH}$ frame centered on CoM of the target. The $\hat{i}$ and $\hat{j}$ axes lie on the orbital plane of motion, with $\hat{i}$ on the same direction of $\boldsymbol{R}$ and $\hat{j}$ perpendicular to $\hat{i}$. The co-moving satellite centered frame is completed by the $\hat{k}$ axis perpendicular to both $\hat{i}$ and $\hat{j}$ according to right hand rule. The relative position vector $\delta\boldsymbol{r}$ is defined as:

$$\delta\boldsymbol{r} = \boldsymbol{r} - \boldsymbol{R} \tag{1}$$

The non-linear equations of motion relative to $\boldsymbol{I}_{LVLH}$ of the chaser are written as in Equation(2) [33]:

$$m_c\delta\ddot{\boldsymbol{r}} + \boldsymbol{C}_t(\dot{\theta})\delta\dot{\boldsymbol{r}} + \boldsymbol{D}_t(\dot{\theta},\ddot{\theta},r)\delta\boldsymbol{r} + \boldsymbol{n}_t(\boldsymbol{r},\boldsymbol{R}) = \boldsymbol{f}_c + \boldsymbol{f}_d \tag{2}$$

where m_c is the chaser mass, θ is the target true anomaly,

$$\boldsymbol{C}_t(\dot{\theta}) = 2m_c\dot{\theta}\begin{bmatrix} 0 & -1 & 0 \\ 1 & 0 & 0 \\ 0 & 0 & 0 \end{bmatrix} \tag{3}$$

is the matrix related to the Coriolis acceleration acting on the target,

$$\boldsymbol{D}_t(\ddot{\theta},\dot{\theta},\boldsymbol{r}) = m_c\begin{bmatrix} \frac{\mu}{r^3} - \dot{\theta} & -\ddot{\theta} & 0 \\ \ddot{\theta} & \frac{\mu}{r^3} - \dot{\theta} & 0 \\ 0 & 0 & \frac{\mu}{r^3} \end{bmatrix} \tag{4}$$

is the time varying matrix related to the potential force, with $r = ||\boldsymbol{r}||$, whereas $\boldsymbol{n}_t$ represents the difference of the gravity effect due to small distances, given by:

$$\boldsymbol{n}_t(\boldsymbol{r},\boldsymbol{R}) = m_c\mu\left[\frac{R}{r^3} - \frac{1}{R^2}, 0, 0\right]^T \tag{5}$$

Finally, $\boldsymbol{f}_c$ and $\boldsymbol{f}_d$ are the control and disturbance force vectors, respectively, with $R = ||\boldsymbol{R}||$.

B. Attitude Dynamics

The relative attitude dynamics is given in the chaser frame [33] according to Equation (6):

$$\boldsymbol{J}_c\dot{\boldsymbol{\omega}} + \boldsymbol{C}_r(\boldsymbol{\omega},\boldsymbol{q})\boldsymbol{\omega} + \boldsymbol{n}_r(\boldsymbol{\omega},\boldsymbol{q}) = \boldsymbol{t}_c + \boldsymbol{t}_d \tag{6}$$

$$\begin{aligned}\boldsymbol{C}_r(\boldsymbol{\omega},\boldsymbol{q}) = {} & \boldsymbol{J}_c\boldsymbol{S}(\boldsymbol{R}_{tb}^{cb}\boldsymbol{\omega}_{i,tb}^{tb}) + \boldsymbol{S}(\boldsymbol{R}_{tb}^{cb}\boldsymbol{\omega}_{i,tb}^{tb})\boldsymbol{J}_c \\ & - \boldsymbol{S}(\boldsymbol{J}_c(\boldsymbol{\omega} + \boldsymbol{R}_{tb}^{cb}\boldsymbol{\omega}_{i,tb}^{tb}))\end{aligned} \tag{7}$$

$$\begin{aligned}\boldsymbol{n}_r(\boldsymbol{\omega},\boldsymbol{q}) = {} & \boldsymbol{S}(\boldsymbol{R}_{tb}^{cb}\boldsymbol{\omega}_{i,tb}^{tb})\boldsymbol{J}_c\boldsymbol{R}_{tb}^{cb}\boldsymbol{\omega}_{i,tb}^{tb} \\ & - \boldsymbol{J}_c\boldsymbol{R}_{tb}^{cb}\boldsymbol{J}_t^{-1}\boldsymbol{S}(\boldsymbol{\omega}_{i,tb}^{tb})\boldsymbol{J}_t\boldsymbol{\omega}_{i,tb}^{tb}\end{aligned} \tag{8}$$

where $\boldsymbol{\omega}$ is the relative angular velocity between $\boldsymbol{I}_{tb}$ and $\boldsymbol{I}_{cb}$ [41], S is the cross product operator i.e. $S(\boldsymbol{q}) = \boldsymbol{q}\times$, $\boldsymbol{R}_{cb}^{tb}$ is the rotation matrix from $\boldsymbol{I}_{cb}$ to $\boldsymbol{I}_{tb}$, $\boldsymbol{\omega}_{i,tb}^{tb}$ is the angular velocity of $\boldsymbol{I}_{tb}$ relative to $\boldsymbol{I}_{\oplus}$ expressed into $\boldsymbol{I}_{tb}$, and $\boldsymbol{q}$ is the relative quaternion between $\boldsymbol{I}_{tb}$ and $\boldsymbol{I}_{cb}$ as defined in [41].

C. Complete Model for Rendezvous

Combining Equations (2) and (6), it is possible to derive the full system of equations that describes the rendezvous approach:

$$\begin{cases} \delta\ddot{\boldsymbol{r}} = -\frac{1}{m_c}\boldsymbol{D}_t\delta\boldsymbol{r} - \frac{1}{m_c}\boldsymbol{C}_t\delta\dot{\boldsymbol{r}} - \frac{1}{m_c}\boldsymbol{n}_t + \frac{1}{m_c}\boldsymbol{f}_c + \frac{1}{m_c}\boldsymbol{f}_d \\ \dot{\boldsymbol{\omega}} = -\boldsymbol{J}_c^{-1}\boldsymbol{C}_r\boldsymbol{\omega} - \boldsymbol{J}_c^{-1}\boldsymbol{n}_r + \boldsymbol{J}_c^{-1}\boldsymbol{t}_c + \boldsymbol{J}_c^{-1}\boldsymbol{t}_d \end{cases} \tag{9}$$

Considering $\delta\dot{\boldsymbol{r}} = \boldsymbol{v}$ and $\dot{\boldsymbol{q}} = \frac{1}{2}\boldsymbol{T}\boldsymbol{\omega}$, it is possible to derive the state - space representation of the system as follows:

$$\dot{\boldsymbol{x}} = \begin{bmatrix} \delta\dot{\boldsymbol{r}} \\ \dot{\boldsymbol{v}} \\ \dot{\boldsymbol{q}} \\ \dot{\boldsymbol{\omega}} \end{bmatrix} = \begin{bmatrix} \boldsymbol{0} & \boldsymbol{I} & \boldsymbol{0} & \boldsymbol{0} \\ -\frac{1}{m_c}\boldsymbol{D}_t & -\frac{1}{m_c}\boldsymbol{C}_t & \boldsymbol{0} & \boldsymbol{0} \\ \boldsymbol{0} & \boldsymbol{0} & \boldsymbol{0} & \frac{1}{2}\boldsymbol{T} \\ \boldsymbol{0} & \boldsymbol{0} & \boldsymbol{0} & -\boldsymbol{J}_c^{-1}\boldsymbol{C}_r \end{bmatrix} \begin{bmatrix} \delta\boldsymbol{r} \\ \boldsymbol{v} \\ \boldsymbol{q} \\ \boldsymbol{\omega} \end{bmatrix} - \begin{bmatrix} \boldsymbol{0} \\ \frac{1}{m_c}\boldsymbol{n}_t \\ \boldsymbol{0} \\ \boldsymbol{J}_c^{-1}\boldsymbol{n}_r \end{bmatrix} + \begin{bmatrix} \boldsymbol{0} \\ \frac{1}{m_c}\boldsymbol{f}_c \\ \boldsymbol{0} \\ J_c^{-1}\boldsymbol{t}_c \end{bmatrix} \tag{10}$$

where $\boldsymbol{f}_c = \boldsymbol{F}_a\boldsymbol{f}_a$ and $\boldsymbol{t}_c = \boldsymbol{T}_a\boldsymbol{f}_a$. $\boldsymbol{F}_a$ and $\boldsymbol{T}_a$ are the matrices that represent the thruster configuration that define the control force and control torque vectors $\boldsymbol{f}_c$ and $\boldsymbol{t}_c$. Considering the thruster configuration, matrices Equation (10) can be written in a more compact notation:

$$\dot{\boldsymbol{x}} = \boldsymbol{A}\boldsymbol{x} - \boldsymbol{n}_d + \boldsymbol{B}\boldsymbol{f}_a \tag{11}$$

where $\boldsymbol{A}$ is the state matrix, $\boldsymbol{n}_d$ is the vector of the disturbances, $\boldsymbol{B}$ is the input matrix, and $\boldsymbol{f}_a$ is the vector of forces generated by thrusters.

D. Linearized Translational Dynamics

The full dynamic model for a rendezvous as described in Equation (10) is highly non linear and needs to be linearized to use standard controllers [42]. The chaser motion in the $\boldsymbol{I}_\oplus$ frame can be computed using Newton gravitational law [43]:

$$\ddot{\boldsymbol{r}} = \boldsymbol{f}_g(\boldsymbol{r}) + \frac{\boldsymbol{F}}{m_c} \tag{12}$$

where $\ddot{\boldsymbol{r}}$ is the acceleration of the chaser, $\boldsymbol{f}_g(\boldsymbol{r})$ is the Newton gravitational acceleration, $\boldsymbol{F}$ are perturbations acting on the chaser and m_c is the mass of the chaser. The motion of the target in the $\boldsymbol{I}_\oplus$ frame can be computed as follows:

$$\ddot{\boldsymbol{R}} = \boldsymbol{f}_g(\boldsymbol{R}) \tag{13}$$

where $\ddot{\boldsymbol{R}}$ is the acceleration of the target and $\boldsymbol{f}_g(\boldsymbol{R})$ is the acceleration due to Newton gravitational law. Substituting equations 12 and 13 into Equation 1 derived twice with respect to time, the relative motion equation reads:

$$\ddot{\boldsymbol{\delta r}} = \boldsymbol{f}_g(\boldsymbol{r}) - \boldsymbol{f}_g(\boldsymbol{R}) + \frac{\boldsymbol{F}}{m_c} \tag{14}$$

$\boldsymbol{f}_g(\boldsymbol{r})$ can be linearized with a Taylor series stopped at the first order around the Target position $\boldsymbol{R}$. Such linearization makes Equation 14 read:

$$\ddot{\boldsymbol{\delta r}} = \boldsymbol{f}_g(\boldsymbol{R}) + \left.\frac{d\boldsymbol{f}_g(\boldsymbol{r})}{d\boldsymbol{r}}\right|_{\boldsymbol{r}=\boldsymbol{R}}(\boldsymbol{r}-\boldsymbol{R}) - \boldsymbol{f}_g(\boldsymbol{R}) + \frac{\boldsymbol{F}}{m_c} \tag{15}$$

where the gravity acceleration at the target position cancels out and $\boldsymbol{r} - \boldsymbol{R} = \boldsymbol{\delta r}$. Computing the partial derivatives considering $\boldsymbol{r} = \boldsymbol{R}$, the relative acceleration of the chaser satellite with respect to the target in the Earth frame $\boldsymbol{I}_\oplus$ reads:

$$\ddot{\boldsymbol{\delta r}} = -\frac{\mu}{r^3}\boldsymbol{M}\boldsymbol{\delta r} + \frac{\boldsymbol{F}}{m_c} \tag{16}$$

where

$$\boldsymbol{M} = \begin{bmatrix} 1 - 3\frac{r_x^2}{r^2} & \frac{3r_xr_y}{r^2} & \frac{3r_xr_z}{r^2} \\ \frac{3r_yr_x}{r^2} & 1 - 3\frac{r_y^2}{r^2} & \frac{3r_yr_z}{r^2} \\ \frac{3r_zr_x}{r^2} & \frac{3r_zr_y}{r^2} & 1 - 3\frac{r_z^2}{r^2} \end{bmatrix} \tag{17}$$

where $r = ||\boldsymbol{r}||$. Equation (16) can be computed relative to $\boldsymbol{I}_{LVLH}$ frame centered on the CoM of the target considering the following equation [44]:

$$\begin{aligned} \frac{d^2\boldsymbol{\delta r}}{dt^2} =& \frac{d^2\boldsymbol{\delta r}_{rel}}{dt^2} + \boldsymbol{\omega}\times(\boldsymbol{\omega}\times\boldsymbol{\delta r}_{rel}) + 2\boldsymbol{\omega}\times\frac{d\boldsymbol{\delta r}_{rel}}{dt} \\ &+ \frac{d\boldsymbol{\omega}}{dt}\times d\boldsymbol{\delta r}_{rel} \end{aligned} \tag{18}$$

where $\boldsymbol{\delta r}_{rel}$ and its time derivatives are referred to $\boldsymbol{I}_{LVLH}$ rotating with an angular rate of $\boldsymbol{\omega}$. Combining Equation (16) and (18) it is possible to compute the linearized equation of motion in the LVLH frame:

$$\begin{aligned} &\frac{d^2\boldsymbol{\delta r}_{rel}}{dt^2} + \boldsymbol{\omega}\times(\boldsymbol{\omega}\times\boldsymbol{\delta r}_{rel}) + 2\boldsymbol{\omega}\times\frac{d\boldsymbol{\delta r}_{rel}}{dt} \\ &+ \frac{d\boldsymbol{\omega}}{dt}\times d\boldsymbol{\delta r}_{rel} + \frac{\mu}{r^3}\boldsymbol{M}\boldsymbol{\delta r}_{rel} = \frac{\boldsymbol{F}}{m_c} \end{aligned} \tag{19}$$

considering angular momentum constant, the orbit circular and performing the vectorial multiplications in Equation (19) it is possible to derive the Hill's equations[45]:

$$\begin{cases} \ddot{x} - 3\frac{\mu}{R^3}x - 2\sqrt{\frac{\mu}{R^3}}\dot{y} = \frac{\boldsymbol{F}_x}{m_c} \\ \ddot{y} + 2\sqrt{\frac{\mu}{R^3}}\dot{x} = \frac{\boldsymbol{F}_y}{m_c} \\ \ddot{z} + \frac{\mu}{R^3}z = \frac{\boldsymbol{F}_z}{m_c} \end{cases} \tag{20}$$

Equation (20) contains the linearized translation dynamics of a rendezvous, which results in state transition matrix being not time dependent, so the term $\boldsymbol{n}_d$ disappears. The homogeneous solution of Equations 20 is the well known Clohessey-Wiltshire equations that are going to be used in section V to simulate the reference trajectory. Note that Equation (11) also includes the attitude dynamics, although its derivation is out of the scope of this paper.

IV. Fully Actuated Multi-Rotor Platform

A. Dynamic Model

The dynamic model of the fully-actuated multi-rotor can be derived from the Euler-Lagrange formulation [20]. The vector of generalized coordinates $\boldsymbol{\xi} = [\boldsymbol{R}\ \ \boldsymbol{\eta}]^\top \in \mathbb{R}^6$ includes the position of the platform's center of gravity, $\boldsymbol{R}$, expressed in $\boldsymbol{I}_\oplus$, and the Euler angles of the attitude, $\boldsymbol{\eta} = [\phi,\ \theta,\ \psi]$, expressed $\boldsymbol{I}_{cb}$. The equations of motion can then be expressed in the standard matrix form:

$$\boldsymbol{M}(\boldsymbol{\xi})\ddot{\boldsymbol{\xi}} + \boldsymbol{C}(\boldsymbol{\xi},\dot{\boldsymbol{\xi}})\dot{\boldsymbol{\xi}} + \boldsymbol{G}(\boldsymbol{\xi}) = \boldsymbol{R}_B\boldsymbol{F}_C + \boldsymbol{F}_{Ext} \qquad (21)$$

where $\boldsymbol{G}(\boldsymbol{\xi})$ includes the gravitational forces, $\boldsymbol{M}(\boldsymbol{\xi})$ is the inertia matrix and $\boldsymbol{C}(\boldsymbol{\xi},\dot{\boldsymbol{\xi}})$ represents the centrifugal and Coriolis terms. Then, $\boldsymbol{F}_C$ is composed of the forces and torques generated by the actuators, whereas $\boldsymbol{F}_{Ext}$ includes the external wrenches, like the contact forces raised in docking maneuvers, or those generated by the wind. Moreover, $\boldsymbol{R}_B = [\boldsymbol{R}_{WB}\ \mathbf{0}_{3\times3};\ \ \mathbf{0}_{3\times3}\ \ \boldsymbol{I}_{3\times3}] \in \mathbb{R}^{6\times6}$ incorporates the rotation matrix $\boldsymbol{R}_{WB} \in \mathbb{R}^{3\times3}$ which allows to express the control vector $\boldsymbol{F}_C$ from the body frame into the world frame. The vector $\boldsymbol{F}_C$ can be expressed as follows:

$$\boldsymbol{F}_C = \begin{bmatrix}\boldsymbol{F}_M \\ \boldsymbol{\tau}_M\end{bmatrix} \in \mathbb{R}^6 \qquad (22)$$

where $\boldsymbol{F}_M = \begin{bmatrix}F_x\ F_y\ F_z\end{bmatrix}^\top$ and $\boldsymbol{\tau}_M = \begin{bmatrix}\tau_\phi\ \tau_\theta\ \tau_\psi\end{bmatrix}^\top \in \mathbb{R}^3$ are the force/torque vectors generated by the propellers, related to the rotational speed ω_i of the rotors as follows:

$$\begin{bmatrix}\boldsymbol{F}_M \\ \boldsymbol{\tau}_M\end{bmatrix} = \begin{bmatrix}F_x \\ F_y \\ F_z \\ \tau_\phi \\ \tau_\theta \\ \tau_\psi\end{bmatrix} = \underbrace{\begin{bmatrix}\boldsymbol{A}_{3\times6}C_T \\ \boldsymbol{B}_{3\times6}LC_T + \boldsymbol{C}_{3\times6}C_D\end{bmatrix}}_{\boldsymbol{H}_{6\times6}} \begin{bmatrix}\omega_1^2 \\ \omega_2^2 \\ \omega_3^2 \\ \omega_4^2 \\ \omega_5^2 \\ \omega_6^2\end{bmatrix} \qquad (23)$$

where the mixer matrix $\boldsymbol{H}_{6\times6}$ [23] has full rank, allowing decoupled position and attitude control. This matrix depends on C_T, C_D and L which are respectively the thrust coefficient of the propeller, the drag coefficient of the propeller, and the distance from the CoM to the rotor position. Matrices $\boldsymbol{A}_{3\times6}$, $\boldsymbol{B}_{3\times6}$ and $\boldsymbol{C}_{3\times6}$ depends on the tilted angles of the motors α and β, computed as indicated in [23].

B. Control Scheme

The simulation of the proximity maneuver carried out by the chaser multi-rotor emulating the orbital flight, described in Section III, relies on the control scheme depicted in Figure 4. As mentioned before, the fully actuated configuration allows to decouple the position and attitude control, implemented as a position-velocity cascade scheme by the ArduPilot software. The attitude controller of he multi-rotor will emulate the effect of reaction wheels or other spacecraft attitude control systems. An extended Kalman filter (EKF) provides the state estimates based on the IMU data and the position measurements given by the Opti-Track positioning system of the testbed. The Chaser Orbital Trajectory Generation block provides the position and attitude references given by Equation (20). Different mass/inertia values of the satellite may be simulated as long as the resulting linear and angular velocities are within the limits of the multi-rotor and there is no physical interaction with the target platform (contact-docking is not considered here). It is assumed that this, implementing the same control architecture as the chaser, is hovering at fixed position, corresponding to the reference frame with respect to which the trajectory is expressed.

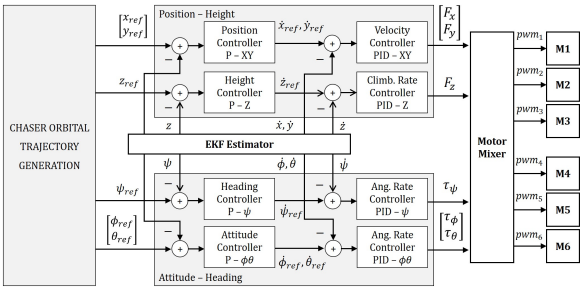

Fig. 4. Control scheme of the chaser fully-actuated multi-rotor comprising the generation of the orbital trajectory relative to the target (left block) and the positon/attitude decoupled cascade controller (right par).

C. Model Comparison

The comparison of Equations (2) and (21) evidences the analogy in the dynamics of the aerial and space platforms expressed by the mass/inertia, Coriolis, and potential terms. The force and torque control vectors of the spacecraft, $\mathbf{f}_c$ and $\mathbf{t}_c$ in Equation (10), are also equivalent to the propellers wrench $\mathbf{F}_C$ given by Equation (22). The effects of microgravity, solar radiation, magnetic field, and other factors that may disturb the spacecraft, can be lumped on the external wrenches $\mathbf{F}_{Ext}$ in Equation (21). Gravity compensation in the aerial platform is implemented by the altitude controller in Figure 4, incorporating the linearized equations of motion given by the orbital mechanics (Equation (20)) in the corresponding trajectory generation block.

V. EXPERIMENTAL RESULTS

A. Benchmarking Multi-rotor Decoupled Dynamics

The goal of this first experiment is to benchmark the fully-actuated multi-rotor to validate its suitability for simulating orbital flights by executing a circular trajectory, decoupling the translation and attitude dynamics as described in Section IV. The experiment, illustrated in Figure 1 and Figure 5 (see also video attachment), consists of completing three circular orbits with zero attitude (roll-pitch), maintaining the orientation towards the Earth, representing the operation of a telecommunication satellite. The orbit of radius 1.8 m is completed in 30 seconds. The standard deviation of the roll and pitch angles is below 1 degree, and the accuracy and repeatability in the trajectory tracking is around 0.2 m.

B. Orbital Flight Simulation

The test presented here simulates the proximity trajectory of the servicer multi-rotor towards the target multi-rotor, implementing the orbital mechanics described in Section III on the scheme shown in Figure 4. A stationary drone is located at the center of the test-bed representing the target satellite at position $\boldsymbol{O} = [0,0,0]$, whereas the chaser satellite is located at initial position $\boldsymbol{r}_0 = [4.3743, 2.4216, 1.0178]\,m$ with a magnitude of $|\boldsymbol{r}_0| = 5.1024\ m$. Chaser and target are assumed to be on a circular orbit around the Earth with initial positions $\boldsymbol{R}_0 = [1622.341, 5310.122, 3750.451]\ km$, $\boldsymbol{r}_0 = [1622.340, 5310.125, 3750.455]\ m$ and velocities $\boldsymbol{V} = [-7.29936, 0.492329, 2.48304]\ km/s$, $\boldsymbol{v} =$

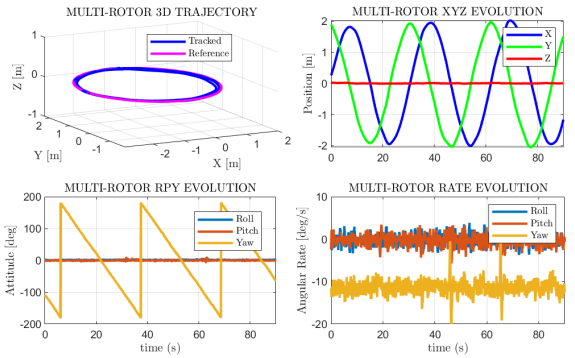

Fig. 5. Orbital trajectory tracked by the fully-actuated multi-rotor satellite for evaluating the translational/attitude decoupling.

$[-7.35170, 0.463828, 2.46906]$ km/s expressed in $\boldsymbol{I}_{\oplus}$. The orbital maneuver is designed in $\boldsymbol{I}_{LVLH}$ where the target is seen stationary and the chaser moves accordingly to the homogeneous solution of the Hill's Equation (20). The initial position of the chaser with respect to the target is $\boldsymbol{\delta r} = [4.3743, 2.4216, 1.0178]$ m which corresponds to the position of the chaser drone in the test-bed. The first impulse maneuver given at $t = 0$ allows the chaser to be put on a different trajectory with respect to its initial one, while the second impulse maneuver is given when the chaser reaches the target at the center of $\boldsymbol{I}_{LVLH}$. Figure 6 shows drone trajectory followed in the testbed along with the simulated trajectory obtained integrating Equation (20) before the stopping point 0.74 m away from the target drone. Such stopping event is necessary due to the docking maneuvers being initiated at a safe distance [46]. To measure

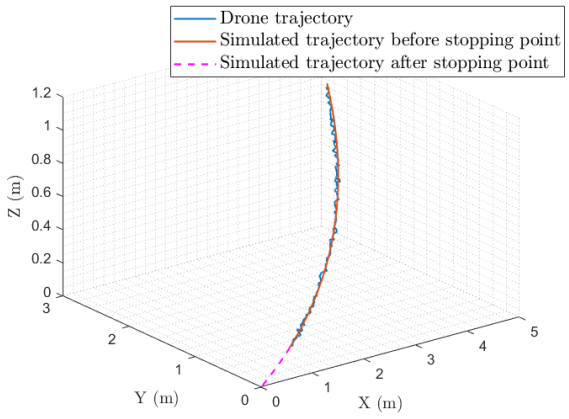

Fig. 6. Overlapping simulated and experimental trajectories.

the performance of the controller, the error between the reference trajectory and the drone trajectory has been computed as the Euclidean norm of the difference between the reference and the observed position at each time step, given by $err = |\boldsymbol{r}_{ref} - \boldsymbol{r}_{obs}|$, where $\boldsymbol{r}_{ref}$ is the drone simulated trajectory and $\boldsymbol{r}_{obs}$ is its observed position. Figure 7 shows the results of the computations. On the same plot, samples are represented by the blue circles and their linear regression with the orange line. The dotted magenta lines above and below the linear fit show the 95% prediction interval. Final approaching maneuvers before docking require an accuracy of the order of cm for docking and m for berthing [46]. The highest error in the sample vector is below 16 cm. As the long term scope of this work is to design the approaching phase before the docking, the precision of the drone testbed is suitable for representing this kind of operations.

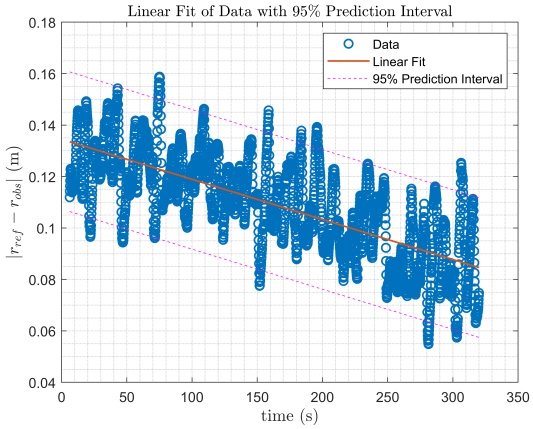

Fig. 7. Linear Fit of Data with 95% Prediction Interval

VI. CONCLUSIONS AND FUTURE WORK

This paper addressed the problem of simulating on-orbit rendezvous proximity operations between a chaser and a target satellite using fully-actuated multi-rotors due to their ability to decouple translational and attitude dynamics, and motivated by the similarities of these flying platforms in both aerial and space domains. The proposed solution is intended to extend the capabilities of existing ground testing facilities, taking benefit of the aerial platforms in terms of floating nature and lower cost compared to current solutions. The paper described a method for implementing the equations of motion of the approaching maneuver taking into account the orbital mechanics, presenting some metrics of interest from the experimental results. As future work, it is considered the realization of a docking maneuver for simulating maintenance or orbit modification operations using two fully-actuated multi-rotors, involving the physical interaction and coordinated control, incorporating on-board perception for guiding the maneuver. It is also desirable to explore the use of omni-directional multi-rotors to allow simulating the full rotation range of the platforms in roll-pitch.

ACKNOWLEDGMENT

This work was supported by the project "Smart Robotics for On- Orbit Servicing Applications (AROSA, CPP-2021-008629)", funded by the Spanish Ministry of Science and Innovation, and by the AEROTRAIN Marie Skłodowska-Curie project (MSCA-ITN-2020-953454), funded by the European Commission.

REFERENCES

[1] C. Oestreich, A. T. Espinoza, J. Todd, K. Albee, and R. Linares, "On-orbit inspection of an unknown, tumbling target using nasa's astrobee robotic free-flyers," in *2021 IEEE/CVF Conference on Computer Vision and Pattern Recognition Workshops (CVPRW)*, pp. 2039–2047, 2021.

[2] E. Stoll, J. Letschnik, U. Walter, J. Artigas, P. Kremer, C. Preusche, and G. Hirzinger, "On-orbit servicing," *IEEE Robotics Automation Magazine*, vol. 16, no. 4, pp. 29–33, 2009.

[3] Z. XUE, J. LIU, C. WU, and Y. TONG, "Review of in-space assembly technologies," *Chinese Journal of Aeronautics*, vol. 34, no. 11, pp. 21–47, 2021.

[4] D. Akin and M. Bowden, "Eva, robotic, and cooperative assembly of large space structures," in *Proceedings, IEEE Aerospace Conference*, vol. 7, pp. 7–7, 2002.

[5] M. Lavagna, L. Bucci, F. Cavenago, and A. Rivolta, "Robotic refueling system for space platform servicing," 10 2015.

[6] V. Svotina and Cherkasova, "Space debris removal â€" review of technologies and techniques. flexible or virtual connection between space debris and service spacecraft," *Acta Astronautica*, vol. 204, pp. 840–853, 2023.

[7] R. Patera, "General method for calculating satellite collision probability," *Journal of Guidance Control and Dynamics - J GUID CONTROL DYNAM*, vol. 24, pp. 716–722, 07 2001.

[8] E. Papadopoulos, F. Aghili, O. Ma, and R. Lampariello, "Robotic manipulation and capture in space: A survey," *Frontiers in Robotics and AI*, p. 228, 2021.

[9] M. Wilde, C. Clark, and M. Romano, "Historical survey of kinematic and dynamic spacecraft simulators for laboratory experimentation of on-orbit proximity maneuvers," *Progress in Aerospace Sciences*, vol. 110, p. 100552, 2019.

[10] W.-J. Li, D.-Y. Cheng, X.-G. Liu, Y.-B. Wang, W.-H. Shi, Z.-X. Tang, F. Gao, F.-M. Zeng, H.-Y. Chai, W.-B. Luo, *et al.*, "On-orbit service (oos) of spacecraft: A review of engineering developments," *Progress in Aerospace Sciences*, vol. 108, pp. 32–120, 2019.

[11] J. L. Schwartz, M. A. Peck, and C. D. Hall, "Historical review of air-bearing spacecraft simulators," *Journal of Guidance, Control, and Dynamics*, vol. 26, no. 4, pp. 513–522, 2003.

[12] M. De Stefano, R. Vijayan, A. Stemmer, F. Elhardt, and C. Ott, "A gravity compensation strategy for on-ground validation of orbital manipulators," pp. 11859–11865, 06 2023.

[13] A. Valmorbida, M. Mazzucato, S. Tronco, S. Debei, and E. C. Lorenzini, "Spartans - a cooperating spacecraft testbed for autonomous proximity operations experiments," in *2015 IEEE International Instrumentation and Measurement Technology Conference (I2MTC) Proceedings*, pp. 739–744, 2015.

[14] S. Deng, J. Zhi, H. Cai, Z. Chen, and Y. Wang, "The design and analysis of light passive air-bearing simulator," in *2022 6th International Conference on Robotics and Automation Sciences (ICRAS)*, pp. 152–156, 2022.

[15] J. Artigas, M. De Stefano, W. Rackl, R. Lampariello, B. Brunner, W. Bertleff, R. Burger, O. Porges, A. Giordano, C. Borst, *et al.*, "The oos-sim: An on-ground simulation facility for on-orbit servicing robotic operations," in *2015 IEEE International Conference on Robotics and Automation (ICRA)*, pp. 2854–2860, IEEE, 2015.

[16] V. Muralidharan, M. R. Makhdoomi, K. R. Barad, L. M. Amaya-Mejía, K. C. Howell, C. Martinez, and M. Olivares-Mendez, "Rendezvous in cislunar halo orbits: Hardware-in-the-loop simulation with coupled orbit and attitude dynamics," *Acta Astronautica*, vol. 211, pp. 556–573, 2023.

[17] M. Chen, L. Zeng, Y. Jin, C. Zhu, Y. Zhang, and X. Zhang, "Design and verification of microgravity simulation system for space station manipulator," in *2021 3rd International Symposium on Robotics Intelligent Manufacturing Technology (ISRIMT)*, pp. 439–444, 2021.

[18] Y. Zhang, J. Richards, J. Hellein, C. Johnson, J. Woodall, T. Sorenson, S. Neelam, A. Ruby, and H. Levine, *NASA's Ground-Based Microgravity Simulation FacilityMicrogravity simulation facility*, vol. 2368, pp. 281–299. 10 2021.

[19] V. Pletser, *Aircraft Parabolic Flights: A Gateway to Orbital Microgravity and Extra-Terrestrial Planetary Gravities*. 05 2020.

[20] S. Rajappa, M. Ryll, H. H. Bülthoff, and A. Franchi, "Modeling, control and design optimization for a fully-actuated hexarotor aerial vehicle with tilted propellers," in *2015 IEEE international conference on robotics and automation (ICRA)*, pp. 4006–4013, IEEE, 2015.

[21] M. Ryll, G. Muscio, F. Pierri, E. Cataldi, G. Antonelli, F. Caccavale, and A. Franchi, "6d physical interaction with a fully actuated aerial robot," in *2017 IEEE International Conference on Robotics and Automation (ICRA)*, pp. 5190–5195, IEEE, 2017.

[22] R. Rashad, J. Goerres, R. Aarts, J. B. Engelen, and S. Stramigioli, "Fully actuated multirotor uavs: A literature review," *IEEE Robotics & Automation Magazine*, vol. 27, no. 3, pp. 97–107, 2020.

[23] P. J. Sanchez-Cuevas, A. Gonzalez-Morgado, N. Cortes, D. B. Gayango, A. E. Jimenez-Cano, A. Ollero, and G. Heredia, "Fully-actuated aerial manipulator for infrastructure contact inspection: Design, modeling, localization, and control," *Sensors*, vol. 20, no. 17, 2020.

[24] D. Brescianini and R. D'Andrea, "Design, modeling and control of an omni-directional aerial vehicle," in *2016 IEEE international conference on robotics and automation (ICRA)*, pp. 3261–3266, IEEE, 2016.

[25] T. Blandino, K. Schroeder, D. Doyle, and J. Black, "Attitude control of an omni-directional aerial vehicle for simulating free-flyer in-space assembly operations," in *AIAA SCITECH 2022 Forum*, p. 0358, 2022.

[26] M. Hamandi, F. Usai, Q. Sablé, N. Staub, M. Tognon, and A. Franchi, "Design of multirotor aerial vehicles: A taxonomy based on input allocation," *The International Journal of Robotics Research*, vol. 40, no. 8-9, pp. 1015–1044, 2021.

[27] E. Kaufman, K. Caldwell, D. Lee, and T. Lee, "Design and development of a free-floating hexrotor uav for 6-dof maneuvers," in *2014 IEEE Aerospace Conference*, pp. 1–10, IEEE, 2014.

[28] M. Peterson, M. Du, B. Springle, and J. Black, "Spacedrones 2.0—hardware-in-the-loop simulation and validation for orbital and deep space computer vision and machine learning tasking using free-flying drone platforms," *Aerospace*, vol. 9, no. 5, p. 254, 2022.

[29] M. Mammarella, E. Capello, M. Lorenzen, F. Dabbene, and F. Allgower, "A general sampling-based smpc approach to spacecraft proximity operations," in *2017 IEEE 56th Annual Conference on Decision and Control (CDC)*, pp. 4521–4526, 2017.

[30] B. Tweddle, A. Saenz-Otero, and D. Miller, "Design and development of a visual navigation testbed for spacecraft proximity operations," *AIAA J.*, 09 2009.

[31] F. Rems, "Integrating the european proximity operations simulator with the formation flying testbed," 01 2012.

[32] H. D. Curtis, *Orbital mechanics for engineering students / Howard D. Curtis*. Elsevier aerospace engineering series, Kidlington, Oxford, UK ; Burlington, MA: Butterworth-Heinemann, 2nd ed ed., 2010.

[33] Y. Yang, "Coupled orbital and attitude control in spacecraft rendezvous and soft docking," *Proceedings of the Institution of Mechanical Engineers, Part G: Journal of Aerospace Engineering*, vol. 233, pp. 3109–3119, aug 2018.

[34] P. Cao, J. Strawson, T. Bewley, and F. Kuester, "Decoupled translational and rotational flight control designs of canted-rotor hexacopters," 01 2021.

[35] D. Yeo, E. Shrestha, D. A. Paley, and E. M. Atkins, *An Empirical Model of Rotorcrafy UAV Downwash for Disturbance Localization and Avoidance*.

[36] R. E. Kalman, "A new approach to linear filtering and prediction problems," *Transactions of the ASME–Journal of Basic Engineering*, vol. 82, no. Series D, pp. 35–45, 1960.

[37] J. Bakarji, J. Callaham, S. L. Brunton, and J. N. Kutz, "Dimensionally consistent learning with buckingham pi," *Nature Computational Science*, vol. 2, no. 12, pp. 834–844, 2022.

[38] L. N. Thai, M. Nahon, and G. Charland-Arcand, "Scaling effects on controllers for multirotors," in *2020 International Conference on Unmanned Aircraft Systems (ICUAS)*, pp. 762–770, IEEE, 2020.

[39] A. Suarez, R. Salmoral, A. Garofano-Soldado, G. Heredia, and A. Ollero, "Aerial device delivery for power line inspection and maintenance," in *2022 International Conference on Unmanned Aircraft Systems (ICUAS)*, pp. 30–38, IEEE, 2022.

[40] M.-F. Loutre, *Precession, Climatic*, pp. 825–826. Dordrecht: Springer Netherlands, 2009.

[41] K. Raymond, E. Grøtli, P. Nicklasson, and J. Gravdahl, "A model of relative translation and rotation in leader-follower," *Modeling, Identification and Control*, vol. 28, 01 2007.

[42] B. M. Moghaddam and R. Chhabra, "On the guidance, navigation and control of in-orbit space robotic missions: A survey and prospective vision," *Acta Astronautica*, vol. 184, pp. 70–100, 2021.

[43] H. D. Curtis, "Chapter 2 - the two-body problem," in *Orbital Me-*

chanics for Engineering Students (Third Edition) (H. D. Curtis, ed.), pp. 59–144, Boston: Butterworth-Heinemann, third edition ed., 2014.
[44] H. D. Curtis, "Chapter 7 - relative motion and rendezvous," in *Orbital Mechanics for Engineering Students (Third Edition)* (H. D. Curtis, ed.), pp. 367–404, Boston: Butterworth-Heinemann, third edition ed., 2014.
[45] S. Vadali, K. Alfriend, and S. Vaddi, "Hill's equations, mean orbital elements, andformation flying of satellites," vol. 106, pp. 187–203, 01 2000.
[46] W. Fehse, *Automated rendezvous and docking of spacecraft*, vol. 16. Cambridge university press, 2003.